Pergamon

Int. J. Solids Structures Vol. 35, No. 7–8, pp. 637–649, 1998

0020-7683/98 $19.00 + .00

PII: S0020-7683(97)00069-3

A MICRO–MACRO CORRELATION ANALYSIS FOR METAL MATRIX COMPOSITES UNDERGOING MULTIAXIAL DAMAGE

CHINGSHEN LI and F. ELLYIN
Department of Mechanical Engineering, University of Alberta, 4–9 Mechanical Engineering Building, Edmonton, Canada, T6G 2G8

(*Received* 29 *September* 1996; *in revised form* 26 *February* 1997)

Abstract—This three dimensional elastoplastic finite element analysis focuses on the macroscopic response to microscopic damage development, and the correlation of extrinsic multiaxial parameters with the intrinsic damage criteria for metal matrix composites under multiaxial tensile loading. The interface debonding and particle fracture are incorporated in a body centred cubic (BCC) unit cell as a representative volume element of alumina particulate-reinforced 6061 aluminum alloy composites undergoing damage. It is found that the multiaxiality of applied stress increases the amplitude of the critical micro-stresses and changes their location. Plastic deformation in the matrix plays a dominant role in inducing damage, and this is clearly demonstrated through comparing the equi-biaxial loading with a uniaxial one having the same equivalent stress value. Numerical results also show that an energy-based macroscopic damage parameter provides a unique relationship between the uniaxial and multiaxial loadings when correlating the micro-damage in the metal matrix composites. © 1997 Elsevier Science Ltd

1. INTRODUCTION

The increased use of metal matrix composites in high performance structures requires a suitable design methodology under multiaxial loading, as well as a better understanding of the microstructure damage resistance under such a loading condition. Our earlier experimental investigations on Al_2O_3 particulate-reinforced 6061 aluminum alloy have identified tensile and fatigue damage in the form of particle fracture and debonding, and have indicated that this damage is a function of the macroscopic stress state (Li and Ellyin, 1996; Xia and Ellyin, 1996).

The dependency of micro-damage on the multiaxiality of macroscopic stress has also been noted for several other materials. For example, Needleman (1987) has shown that the void nucleation stress at an inclusion is linearly proportional to the hydrostatic tension. Furthermore, the damage-induced dilatation in particulate-reinforced polymer composites is shown to be a function of the hydrostatic pressure (Ravichandran and Liu, 1995). On the other hand, micro-damage results in an anisotropic macroscopic response of metal matrix composites. Lissenden and Herakovich's (1996) experimental results on fibre reinforced titanium matrix composites under multiaxial loading, indicated a different type of response to the axial shear and transverse tensile loading compared to that of the axial tensile loading due to fibre debonding. A different response in the hoop direction to that in the axial direction, is also noted in the tubular specimens of Al_2O_3/6061 composites, once damage develops under a biaxial loading (Xia and Ellyin, 1996).

Equivalent stress and strain energy are mechanics' parameters widely applied in engineering design as well as in damage analysis for ductile materials under multiaxial loading. The equivalent stress demonstrates the combined effect of multiaxial stresses to induce plastic deformation (Marin, 1962). Lemaitre (1986) has correlated the localised damage with the global one by using equivalent stress. Energy-based damage criterion has been applied to predict the macro-crack initiation, e.g.

$$\frac{\mathrm{d}W_e}{2\,\mathrm{d}D} = Y_e \tag{1}$$

in which W_e, D and Y_e are the elastic strain energy, a damage parameter and a material constant, respectively (Lemaitre, 1986). Using the strain energy as a damage function, a constitutive model was developed by Ravichandran and Liu (1995) for an elastic particulate polymeric composite undergoing debonding damage. The strain energy approach has also been widely applied as a damage measure of multiaxial cyclic loading by Ellyin and Xia (1993). It is noteworthy that most of the above studies are restricted to homogeneous materials, mainly, metals and alloys. In particulate-reinforced metal matrix composites (PMMCs), heat-treatment-induced residual stresses (Shi *et al.*, 1993) play an important role in inducing damage in PMMCs (Mochida *et al.*, 1991). It would appear reasonable to investigate the correlation of micro damage in PMMCs under multiaxial loading with these macro parameters, the applied equivalent stress and strain energy.

This investigation aims to provide a better understanding on the correlation of extrinsic damage variables with the intrinsic damage mechanisms for PMMCs, and attempts to bridge the gap between the macroscopic multiaxial damage parameter with the micro-damage mechanism. A body centred cubic unit cell is constructed with the capability to determine the heat treatment-induced residual stresses and a damage-monitoring mechanism, for Al_2O_3 particulate-reinforced 6061 aluminum alloy composite. The interfacial normal stress and the maximum stress at particles are considered as microscopic damage variables. A methodology is employed to reveal the merits of the extrinsic energy-based damage parameter and the equivalent stress parameter in correlating with the intrinsic damage criteria for the PMMCs. This is achieved by comparing the damage developed in the uniaxial loading case with that of an equibiaxial one.

2. MICRO-DAMAGE CRITERIA FOR PMMCS

2.1. *Interface debonding*

The interest in investigating a micro-damage criterion began with the inclusion problem in steels about two decades ago (Argon *et al.*, 1975). There are three types of criterion proposed for the particle (inclusion) debonding: stress-based (Needleman and Rice, 1978; Chang and Asaro, 1978, strain-based (Gurson, 1975) and strain energy-based (Gurland and Plateau, 1963). According to the strain energy criterion, a crack at an interface could form when the locally concentrated elastic strain energy, which is released upon decohesion, becomes comparable to the energy required to create a new surface. On the other hand, Chang and Asaro's (1978) stress criterion, implies that an interface debonding occurs when the local normal stress at the interface, σ_n^i, reaches the interfacial strength, σ_c, i.e.

$$\sigma_n^i = \sigma_c. \tag{2}$$

It is to be noted that the interfacial strength varies with the heat-treatment and particle shape. For iron carbide particles in spheroidized steel, the interfacial strength is about three times as high as the yield strength of the steel (Argon *et al.*, 1975; Cialone and Asaro, 1978). At present, there is no reported data on the interfacial strength of alumina-6061 aluminum alloy composites.

Needleman and Rice (1978) have shown that the particle debonding in a steel depends on the prevailing multiaxial stress state. In PMMCs the particle volume fraction is much higher, and the particle size is generally much larger than in steels. This then induces a higher local stress triaxiality (Shi *et al.*, 1993). Hence, the inter-relation between the local critical stress and the applied stress in the composites would be significantly different from that for steels and alloys. In this study the stress criterion, eqn (2), will be adapted for the debonding in PMMCs, however. we will investigate the dependence of interfacial stresses on the applied stress state.

2.2. *Particle fracture*

Lin *et al.* (1992) have identified stress-controlled failure characteristics for 99.8% alumina cylindrical specimens under tensile and cyclic loading. Several stress-based criteria have been proposed for the multiaxial failure of brittle materials. Although a particle fails in a brittle manner, its fracture characteristic is considerably different from that of the same pure material due to the thermal and deformation constraint of the surrounding matrix.

Particles in a composite are subjected to the thermo-residual stresses, σ_{ij}^r, due to the difference in thermal coefficients of the constituents and the deformation-incompatibility-induced stresses, σ_{ij}^s, i.e.

$$\sigma_{ij}^p = \sigma_{ij}^r + \sigma_{ij}^s \tag{3}$$

where σ_{ij}^r are compressive residual stresses, which may be slightly released under an applied tensile load. The stress components σ_{ij}^s will increase dramatically as the matrix deforms plastically. It is found that for the intermediate or high applied stresses, the maximum principal stress at particles is linearly proportional to the plastic strain (Mochida *et al.*, 1991).

Fracture of particles in composites is affected by several factors, such as the magnitude of residual stress, matrix constraint, cluster distribution, particle size and manufacturing process. These then make it inappropriate to apply directly the criterion for brittle materials to the particle fracture. The fractured particles are also difficult to detect experimentally due to the compressive residual stress at the particles which induces closure (Davidson, 1991). The stress-controlled fracture characteristics have been identified in Al_2O_3/6061 aluminum composites (Lloyd, 1991; 1995) and particulate-reinforced nickel matrix composites (Takehiro *et al.*, 1995). It is also observed that the larger the particle, the more likely it is to fracture under a tensile deformation (Davidson, 1991).

The above experimental results then suggest that a particle fractures under tensile loading when the maximum principal stress at the particle, σ_1^p, exceeds the fracture strength of the particle. However, the fracture strength of a particle is not a constant, it depends on the size, shape and heat-treatment. This study is concerned with the uniaxial and equibiaxial tensile loadings, and we will use σ_1^p as a critical stress for the particle fracture. The magnitude of fracture stress of alumina particles in an aluminum alloy composite, is much higher than the one obtained from a pure alumina polycrystal specimen. Mochida *et al.* (1991) reported the probability of an alumina particle fracture in PMMCs at a stress range of 650 to 850 MPa.

Thus, in the following numerical analysis we will use the maximum interfacial normal stress criterion for debonding, eqn (2), and the maximum principal stress criterion for particle fracture.

3. DESCRIPTION OF THE MODEL

Numerical analyses based on a unit cell model (Dib and Rodin, 1993), or a self-consistent model (Hill, 1965) have been employed to explore the local and overall stress–strain fields of heterogeneous materials. A body centred cubic unit cell was used by Wienecke *et al.* (1995) to study the polycrystal creep, and deformation of particulate-reinforced composites.

The present micro-macro damage analysis also uses a three-dimensional, body centred cubic (BCC) unit cell for Al_2O_3 particulate-reinforced 6061 aluminum alloy composite. In comparison with the simple cubic unit cell, the BCC arrangement of particles represents a denser and more suitable arrangement of particles in the matrix. Moreover, this model can be used to analyze the interaction of particles, and the effect of particle size. In contrast to the previous studies, the particle shape is assumed to be a short cylinder. Therefore, depending on the aspect ratio, this arrangement can also represent a whisker composite. The short cylindrical shape provides a suitable stress concentration factor, it is higher than that with a sphere particle, and lower than a cubic particle.

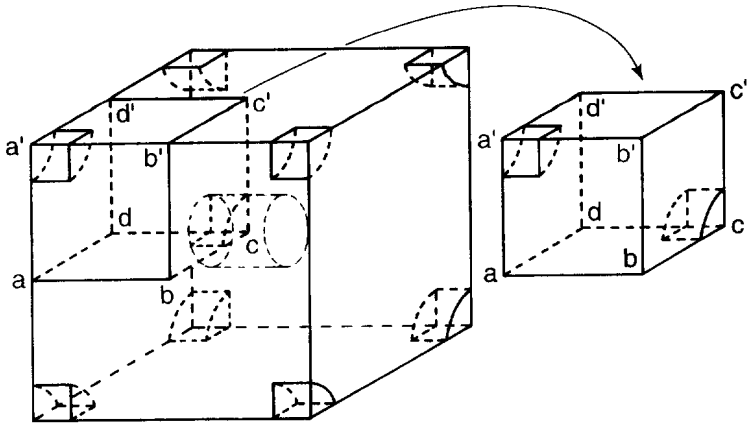

BCC

Fig. 1. One eighth of a body centre cubic unit cell needs to be meshed according to its symmetry and periodic deformation requirement under tensile loading.

To ensure that a BCC unit cell model is a representative volume element of the composite material, it is necessary to enforce boundary conditions which conform to a general periodic deformation condition. Nagpal *et al.* (1972) and Wienecke *et al.* (1995) have specified periodic deformation boundary conditions for two dimension and three dimension deformations, respectively. For face $x_1 = 1$ in the BCC unit cell, with the coordinate origin placed at the centre of the cubic, Fig. 1, we have

$$\mathbf{u}(1, x_2, x_3) = \mathbf{u}(-1, x_2, x_3) + \mathbf{u}(1, 0, 0) - \mathbf{u}(-1, 0, 0). \tag{4}$$

For face $x_2 = 1$ in the unit cell,

$$\mathbf{u}(x_1, 1, x_3) = \mathbf{u}(x_1, -1, x_3) + \mathbf{u}(0, 1, 0) - \mathbf{u}(0, -1, 0). \tag{5}$$

For face $x_3 = -1$ in the unit cell,

$$\mathbf{u}(x_1, x_2, -1) = \mathbf{u}(x_1, x_2, 1) + \mathbf{u}(0, 0, -1) - \mathbf{u}(0, 0, 1). \tag{6}$$

These equations imply no gap (or crack) in the material during and after the deformation. As the BCC unit cell is divided into eight sub cubics, one eighth of it, namely abcda′b′c′d′ as shown in Fig. 1(b) was analysed. A periodic material structure arrangement and a periodic deformation condition of the BCC unit cell are equivalent to the condition that a mirror symmetry exists for the material microstructure and the displacement of the sub unit cells. This then yields the following equations:
for $x_1 = 1$ and $x_1 = -1$ faces,

$$\mathbf{u}_p - \mathbf{u}_d = \mathbf{u}_{p'} - \mathbf{u}_{d'}, \tag{7}$$

where subscripts p and d refer to any two points on $x_1 = 1$ face, and p' and d' are the corresponding, parallel points to p and d on $x_1 = -1$ face. Equation (7) indicates parallel displacements on opposing faces during the deformation process. Similar equations apply for $x_1 = 1$ and $x_2 = -1$ faces, as well as for $x_3 = -1$ and $x_3 = 1$ faces.

The curvature of all cubic faces of the unit cell under tensile loading is negligible, and these faces approximately keep coplanar during deformation. This is experimentally observed by using a plate with periodically located holes (Kujawski *et al.* 1995). Obviously, this coplanar deformation assumption satisfies the periodic deformation requirement for the BCC unit cell. All nodes on the opposite planes are constrained to stay on the same plane during deformation,

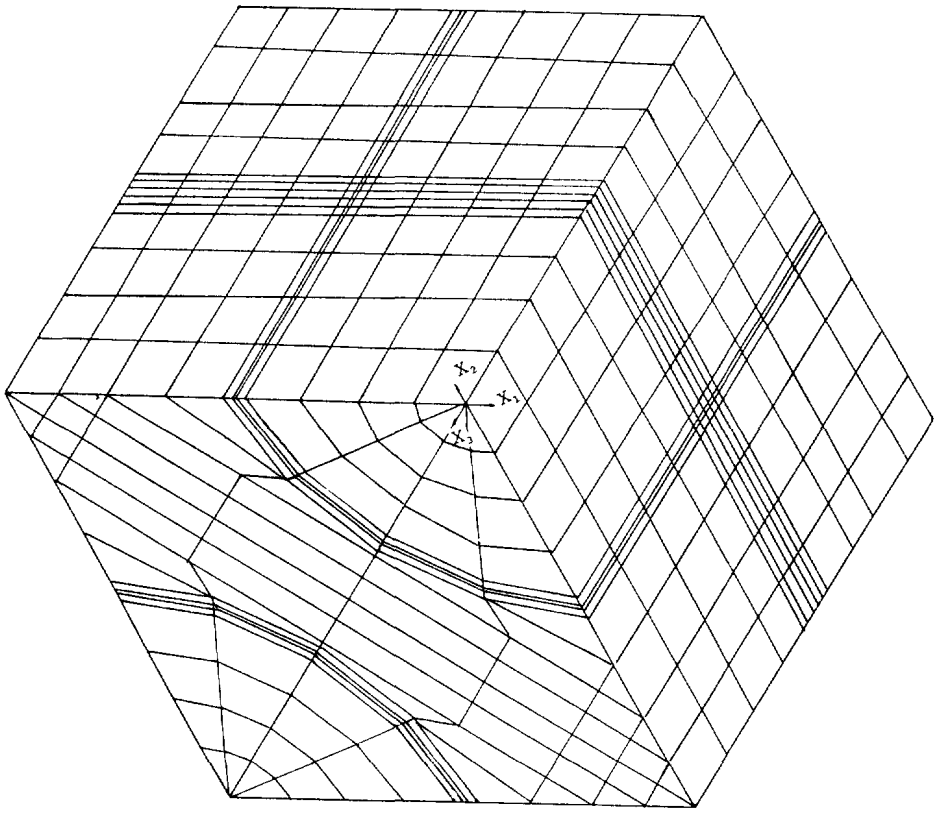

Fig. 2. The finite element mesh for the BCC unit cell, consisting of 1520, 3-D solid elements.

$$u_1(1, x_2, x_3) = C_1$$
$$u_2(x_1, 1, x_3) = C_2$$
$$u_3(x_1, x_2, 1) = C_3 \tag{8}$$

in which C_i is a load-dependent constant. Rigid body motions are eliminated by applying

$$u_1(0, x_2, x_3) = u_2(x_1, 0, x_3) = u_3(x_1, x_2, 0) = 0. \tag{9}$$

This three dimensional model provides a more suitable ratio of interface/volume than a two dimensional model for PMMCs, and the residual stresses and their distribution along the interface can reasonably be predicted (Shi *et al.*, 1993). Figure 2 displays the 3-D finite element mesh which consists of 1520 elements. Thin elements, 0.005 in thickness, are located around the interfaces of particles. The material properties for these elements are the same as that of the matrix. This approach has been applied in modelling of grain boundaries in metallic polycrystals (Li, 1990, 1992). The matrix is assumed to be perfectly bonded to the particles, except when a debonding is modelled. The interfacial strength is dependent on the interface shape and size, and varies across an interface (Needleman, 1987). In this study, the critical interfacial normal stress to cause debonding is assumed to be 3 times the yield stress. The interface debonding is modelled by removing the appropriate number of interface elements where the maximum normal interfacial stress is equal or exceeded the critical interfacial stress.

The mechanical and thermal properties of 6061 aluminum alloy and alumina were taken from Li and Ellyin (1994). The stress–strain curves of the matrix, 6061 aluminum alloy, at 20°C and 500°C were approximated by 5 rectilinear sections. The residual stresses were then induced by applying a temperature drop from 500°C to 20°C (T4 heat-treatment condition) in 20 steps. This temperature drop induces a compressive residual stress with an

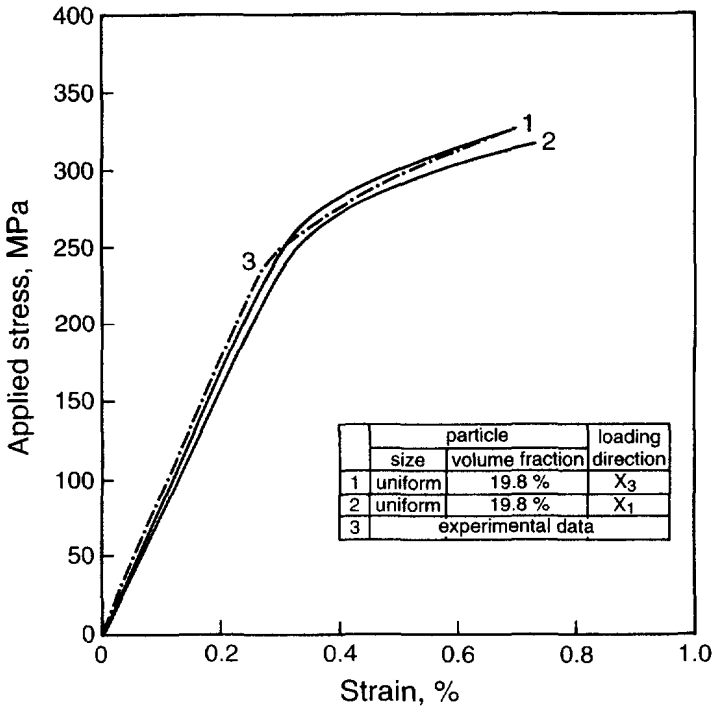

Fig. 3. Stress–strain curves calculated by the finite element model when loaded along x_1 axis (2) or x_3 axis (1), and compared with the experimentally measured curve (3) for 20% Al_2O_3 particulate-reinforced 6061 aluminum alloy under T6 heat-treatment condition.

amplitude of about 400 MPa in the particles, which is approximately equal to that measured by using neutron diffraction (Shi *et al.*, 1993).

A proportional, equibiaxial load was applied as a surface pressure on the $x_1 = 1$ and $x_2 = 1$ planes, while a uniaxial load was simulated by the application of the surface pressure on the $x_1 = 1$ plane. For the sake of comparison, the equivalent stress, or von Mises stress (see eqn 11) for these two loading cases was kept the same. Note however, that the stress triaxiality is different for these two loading cases. This model displays a slight anisotropy along x_3 direction in comparison with the other two directions. The calculated stress–strain curves for x_1 and x_3 loading directions are plotted in Fig. 3. It is seen that the predicted curves are in close agreement with the experimentally measured one of 6061 aluminum alloy reinforced with 20% Al_2O_3 particles under T4 heat-treatment condition.

4. MICRO DAMAGE AND MACRO RESPONSE

4.1. *Location of critical stress and micro damage*

It was mentioned earlier that a temperature drop from 500°C to 20°C induces compressive residual stress at the particles and interfaces of the unit cell. This temperature drop is about the same as the T4 heat-treatment of alumina-reinforced 6061 aluminum composite. The maximum compressive residual stress at the particle is about 400 MPa in absolute value and is located at the particle edge. It was found that under the low applied equivalent stress range ($<0.6\ \sigma_y$) the maximum stress locates at the matrix about the mid-distance between the particles. In other words, the heat-treatment induced compressive residual stresses prevent the interface and the particle from being damaged at the low applied stress. At the intermediate and high applied stress, plastic deformation takes place and the maximum normal interface stress and the maximum principal stress at the particles, are higher than that in the matrix.

The location of the maximum normal interfacial stress or the maximum principal stress, depends on the applied stress state, although it is generally at a section along the

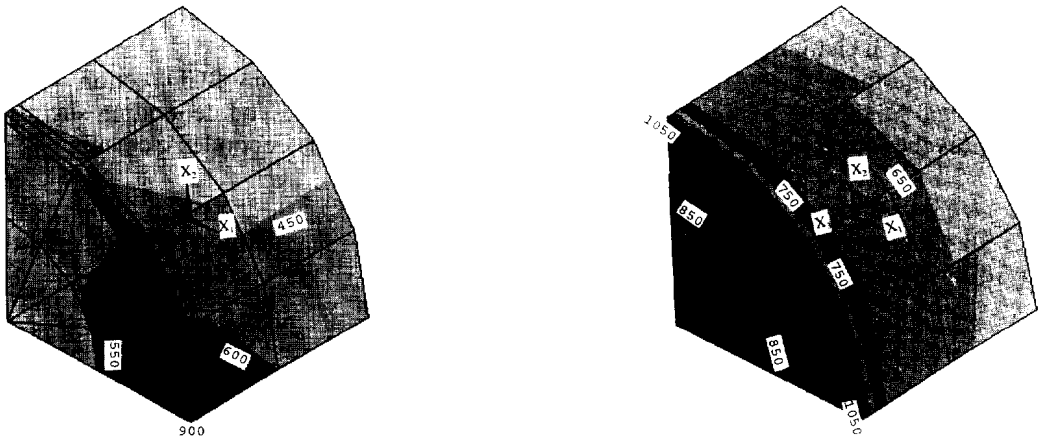

a b

Fig. 4. Distribution of the maximum principal stress at the particle under equibiaxial loading $\sigma_{11} = \sigma_{22} = 290$ MPa(a) and under uniaxial loading $\sigma_{11} = 290$ MPa(b).

interface edge or particle edge. Figures 4a and b display the maximum principal stress at the particle under uniaxial stress $\sigma_{11} = 290$ MPa and equibiaxial stress, $\sigma_{11} = \sigma_{22} = 290$ MPa, respectively. It is seen that the maximum principal stress at particles is much higher under equibiaxial loading than under uniaxial loading of the same equivalent stress value. Moreover, the location of the maximum principal stress in these two cases is different. It is located at two edge corners ($x_1 = 0$ plane, $x_2 = 0$ plane) under equibiaxial loading, while for the uniaxial loading it is at the edge corner near $x_2 = 0$ plane along x_1 axis (see Fig. 2 for the coordinate axes).

The interfacial normal stress under equibiaxial stress is also higher than that under the uniaxial loading of the same equivalent stress value. In the former loading case the maximum normal interfacial stress is symmetrically distributed across the interface edge section (Fig. 5b), while it is located at the corner edge near the $x_2 = 0$ in the later case. Therefore, the location and value of critical stresses are affected by the stress multiaxility of the applied

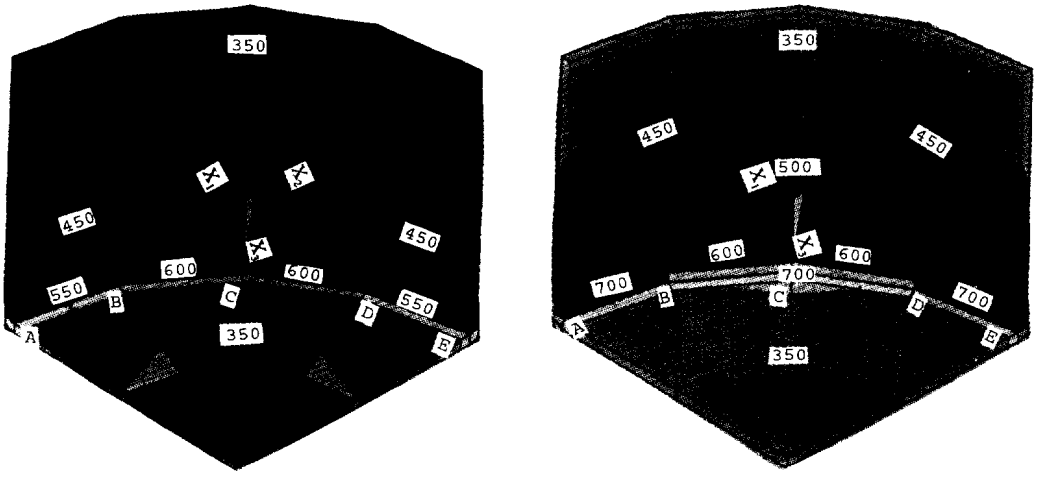

a b

Fig. 5. Distribution of interfacial normal stress at the particle/matrix interface (a) prior to debonding, (b) after debonding at the interface edge centre section BCD under equibiaxial loading $\sigma_{11} = \sigma_{22} = 290$ MPa.

loads. This then indicates the effect of the multiaxiality of applied loads in enhancing damage, and in changing the damage location.

The interfacial normal stress distribution after a debonding along BCD section under equibiaxial loading of $\sigma_{11} = \sigma_{22} = 290$ MPa is shown in Fig. 5b. The debonding slightly enhances the interfacial normal stress at the elements around the debonded elements.

4.2. *Macro-response to micro damage*

Based on a uniform damage distribution assumption, the degradation of elastic modulus of PMMCs would be isotropic, and is given by

$$E' = E(1 - D) \tag{10}$$

in which E is the initial elastic modulus of the material prior to the initiation of damage. Using Eshelby's inclusion model, Mochida *et al.* (1991) have shown that the elastic modulus depends on the fraction of debonded particles in the particulate-reinforced metal matrix composites. However, damage in the PMMCs is anisotropic and loading dependent, therefore, it cannot be properly described by such a simplified model.

In this study, as mentioned previously, the interface debonding is modelled by removing the interface elements around the area of the maximum interfacial normal stress which has exceeded a critical value, and the elastic modulus is calculated by the unloading and reloading of the debonded model. Under a uniaxial loading in the x_1 direction, the maximum interfacial normal stress, hence the debonding, is located at a corner near the $x_2 = 0$ plane. This induces more degradation of E_{x1} than E_{x2} modulus. The equibiaxial loading induces debonding at the section BCD, resulting in the same amount of degradation of E_{x1} as E_{x2} (see Fig. 6). These results show that the materials degradation due to the debonding can be anisotropic, it depends on the applied loads.

Another macroscopic response to the debonded particles in PMMCs is displayed through the stress–strain behaviour of the debonded unit cell after pre-loading. The fraction of the debonded particles in the PMMCs is simulated by the area percentage of the removed interface elements over the interface area. Figure 6 shows the stress–strain curves of this BCC unit cell with 2% interface debonding under uniaxial and equibiaxial loading, both with the maximum applied equivalent stress of 290 MPa. As a result of the induced debonding, a hysteresis loop occurs in Fig. 6. For a unit cell with the same debonded area, a uniaxial load induces a higher plastic strain and a larger hysteresis loop than an equibiaxial

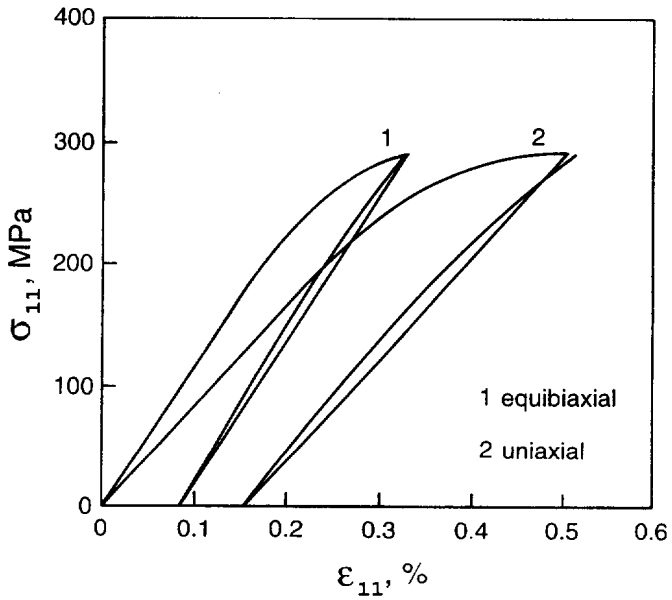

Fig. 6. Comparison of loading-debonding-reloading curves of the model with $\sigma_{11,max} = 290$ for the uniaxial loading and $\sigma_{11,max} = \sigma_{22,max} = 290$ MPa for the equibiaxial loading.

loading of the same equivalent value. As the debonded area increases, the maximum hysteresis loop width increases. This is indicative of the damage development. Similarly, the equibiaxial loading results in loops of the same shape along the x_1 and x_2 axes, but their width is smaller than that under the x_1 uniaxial loading of an equivalent value. However, the total plastic strain energy (the areas of the hysteresis loops) is greater for the equibiaxial loading. Note that the slope of the elastic reloading part is affected by the residual stress/strain pattern in the debonded area.

5. CORRELATION OF MACRO AND MICRO DAMAGE PARAMETERS

The maximum interfacial normal stress and the maximum principal stress at the particle are used as the critical stress criterion for the interface debonding and particle fracture, respectively. These critical stresses under uniaxial and equibiaxial loading are compared with the equivalent stress and strain energy parameters, respectively.

5.1. *Comparison based on the equivalent applied stress*

Equivalent (effective) stress is widely applied in engineering design, and is defined as

$$\sigma_{eqv} = [(\sigma_1-\sigma_2)^2+(\sigma_1-\sigma_3)^2+(\sigma_2-\sigma_3)^2]^{1/2}/\sqrt{2}. \tag{11}$$

It has been demonstrated experimentally that σ_{eqv} determines the ability of multiaxial stress states to induce yielding and plastic flow (e.g., Nadai, 1950).

The maximum interfacial normal stress in the BCC unit cell under equibiaxial loads versus the equivalent applied stress, is shown in Fig. 7, and is compared with that of the uniaxial loading. In the low equivalent stress range the maximum stress is located in the matrix at about mid-distance between the particles. Due to the heat treatment-induced compressive residual stress, the interfacial stress and stress at the particles are low at this level of applied stress.

In the intermediate equivalent stress range, the maximum interfacial normal stress and the maximum principal stress at the particles are higher than those in the matrix. As shown in Fig. 7, the equibiaxial stress induces higher interfacial normal stress than the uniaxial stress of the same equivalent value. Assuming that the interfacial strength in the Al_2O_3/6061

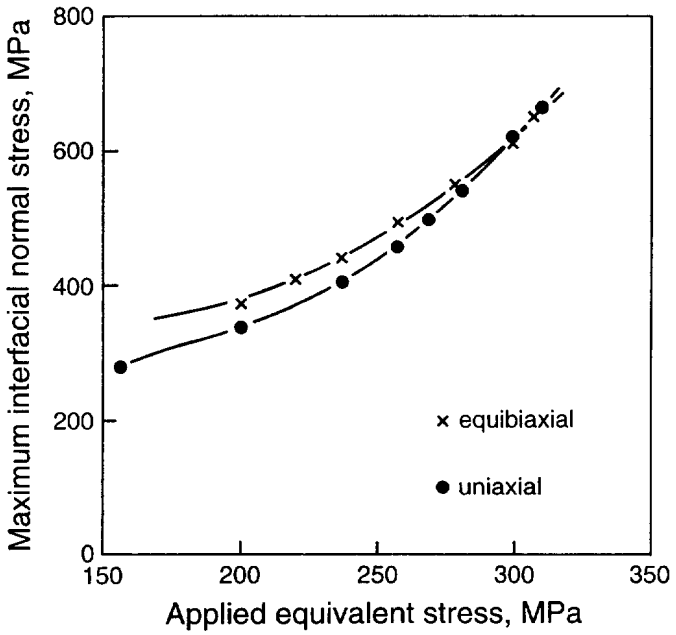

Fig. 7. A plot of the interfacial normal stress vs the equivalent stress showing a higher interfacial normal stress induced under the equibiaxial loading than that of the uniaxial loading of the same applied equivalent stress.

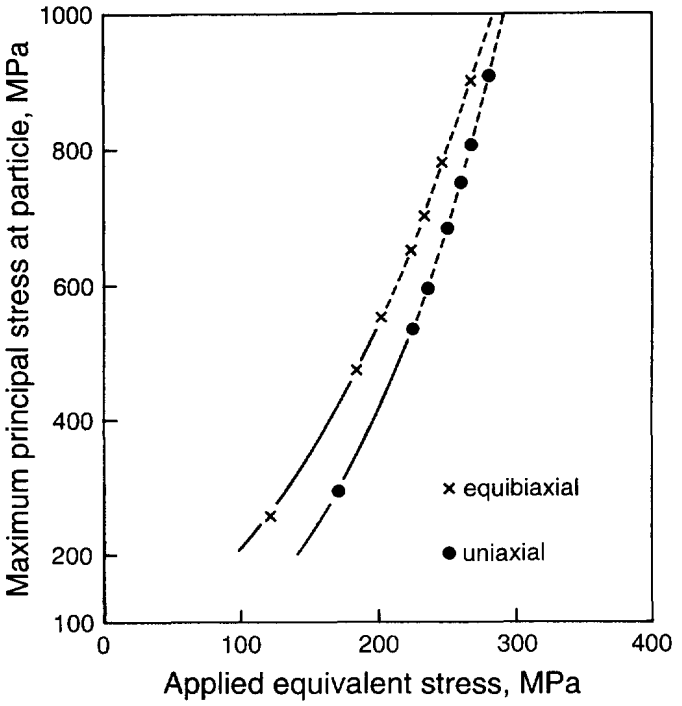

Fig. 8. A plot of the maximum principal stress at particles versus the equivalent applied stress displaying a higher maximin principal stress being induced under the equibiaxial loading than that of the uniaxial loading.

aluminum is about 3 times as high as the yield strength (Needleman, 1987), the minimum applied uniaxial stress to cause interface debonding would be $\sigma_{11} = 250$ MPa, while that for the equibiaxial stress would be $\sigma_{11} = \sigma_{22} = 220$ MPa.

The difference between interfacial normal stress under uniaxial and equibiaxial loading decreases as the applied equivalent stress increases, specially at the high applied equivalent stress where macroscopic plasticity is observed.

A similar trend is also observed for the maximum principal stress at the particles, as depicted in Fig. 8. At a low applied stress, the maximum stress is located in the matrix, while at an intermediate applied stress, the maximum principal stress is at the particles, and it increases with the increase of applied equivalent stress. The maximum principal stress at a particle under equibiaxial loading approaches that of the uniaxial loading with the increased applied equivalent stress, Fig. 8.

It is interesting to note that a biaxial loading of the same equivalent stress value induces a higher interfacial stress and particle stress than a uniaxial one. This is attributed to the existence of a higher stress triaxility in the case of biaxial loading which causes damage in PMMCs.

As shown in Figs 7 and 8, the uniaxial loading data approach that of the equibiaxial loading at the high applied stress values. The accelerated rise of the interfacial normal stress and the maximum principal stress at the particles in the high stress level, is caused by the development of macro-plastic strain and the required compatibility at the interfaces (Li, 1992). This then indicates that plasticity plays an essential role in inducing micro-damage in the PMMCs.

5.2. *Comparison based on the applied strain energy*

The maximum interfacial normal stress of Fig. 7 and the maximum principal stress at particle of Fig. 8 are replotted versus the applied strain energy in Figs 9 and 10, respectively. The applied strain energy is calculated numerically from,

$$W = \int \sigma_{ij}\, d\varepsilon_{ij} \tag{12}$$

which corresponds to the area under the stress–strain curves. Obviously, the strain energy under equibiaxial load is a summation of areas in the two directions (x_1 and x_2).

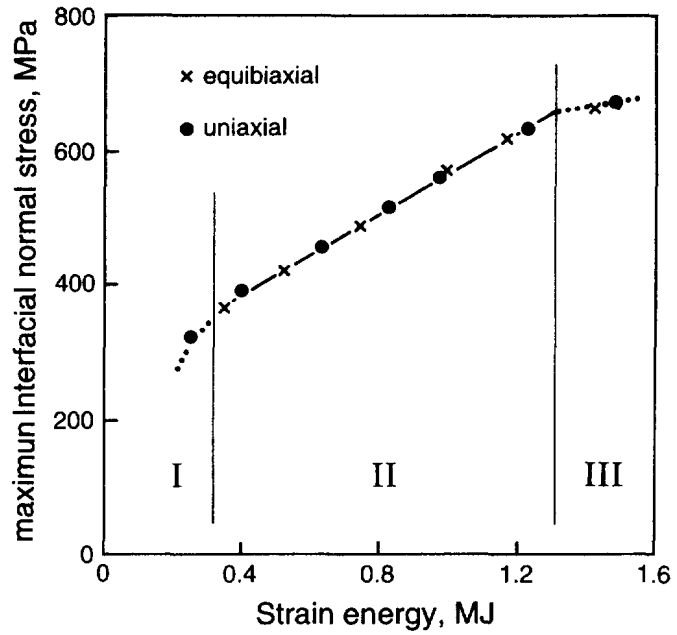

Fig. 9. A replot of the interfacial maximum normal stresses of the data in Fig. 7 vs the applied strain energy.

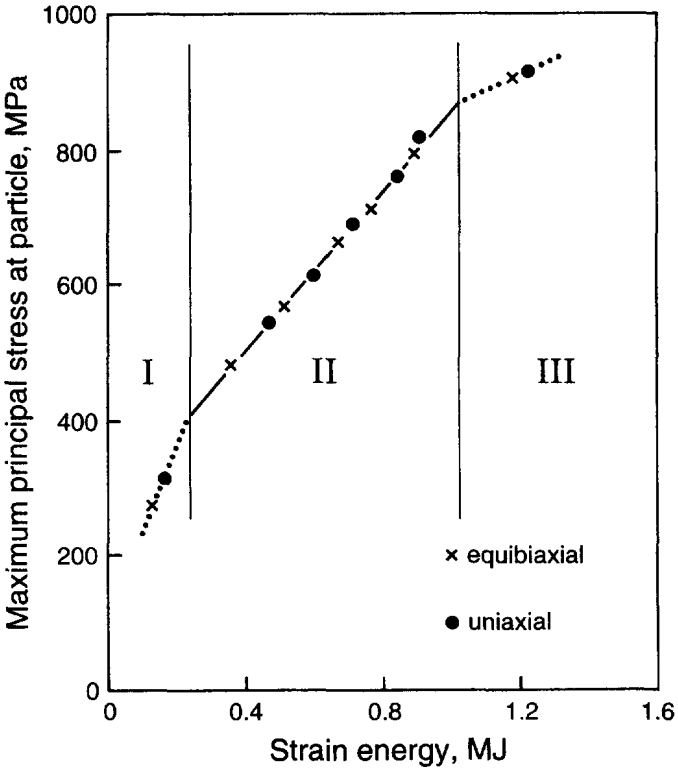

Fig. 10. A replot of the maximum principal stress at the particles of the data in Fig. 8 vs the applied strain energy.

The data in Figs 9 and 10 can be grouped under three fairly distinct sections: a low applied equivalent stress level ($<0.6\sigma_y$), an intermediate applied equivalent stress range ($0.6\sigma_y < \sigma_{eqv} < 1.2\sigma_y$), and a high applied equivalent stress level ($>1.2\sigma_y$). In the low applied equivalent stress level, the micro-plastic strain is very small and the maximum stress is located in the matrix rather than at the interfaces or at the particles.

It is interesting to note that the data under uniaxial and biaxial loadings indicate an almost linear relationship in the intermediate stress range, and the distinction between the uniaxial and biaxial loading disappears when the applied strain energy is used as a correlation parameter (cf. Figs 7 and 9, and Figs 8 and 10). At the high applied stress level, there is a change in slope of the linear relation between the applied strain energy and the maximum normal interfacial stress or the maximum principal stress. Nevertheless, the equibiaxial and the uniaxial data also coincide in this region. From the above one can conclude that the strain energy as a macro damage parameter is a better indicator in correlating the multiaxial with the uniaxial loads for the PMMCs of fixed microstructure, than an equivalent stress parameter.

6. SUMMARY

An elastoplastic damage analysis based on a three dimensional body-centred cubic unit cell with the capability of monitoring the effects of: heat-treatment induced residual stresses, interface-debonding and particle fracture in the particulate-reinforced metal matrix composites, is presented. The maximum interfacial normal stress and the maximum principal stress at the particles are used as microscopic damage criteria for the interface debonding and particle fracture, respectively. Based on this model, a comparative study is conducted to investigate the correlation between the macroscopic damage parameters with the above microscopic criteria for the PMMCs under equibiaxial and uniaxial loadings. The following conclusions are reached:

1. At the low applied stress region (very small micro-plasticity), the maximum stresses are located in the matrix between the particles, the compressive residual stresses at the particles prevent the reinforcement from being damaged.
2. An equibiaxial loading generally induces a higher maximum normal interfacial stress and a higher maximum principal stress at particles than a uniaxial loading of the same equivalent value. This is different from that of the homogeneous materials where the multiaxial loading does not increase the local stresses. Hence, the multiaxility of the applied loads promotes damage in metal matrix composites.
3. The multiaxility of applied stress also causes a change in the location of the maximum interfacial normal stress and the maximum principal stress at the particles. Therefore, damage in the form of interface debonding in PMMCs is anisotropic, and loading-dependent.
4. The applied strain energy parameter provides a unique curve for the equibiaxial loading and uniaxial loading when correlating with the microscopic damage parameters for the PMMCs.
5. At the high applied stress range ($\geqslant 1.2\sigma_y$) the equivalent stress parameter also provides a reasonably good coincidence of the equibiaxial and uniaxial loadings when correlating the micro-critical stress, thus, revealing the dominant role of the plastic strain in the matrix which induces debonding and particle fracture.

Acknowledgement—This research is supported by the Natural Science and Engineering Research Council of Canada (NSERC) under strategic grant No. STR 0149082. Beneficial discussions and comments of Dr David Lloyd of Alcan International is hereby acknowledged.

REFERENCES

Argon, A. S., Im, J. and Safoglu, R. (1975) Cavity formation from inclusions in ductile fracture. *Metallic Transactions* **6A,** 825–830.

Chang, Y. W. and Asaro, R. J. (1978) Bauschinger effects and work hardening in spheroidized steels. *Metal Science* **12,** 277–284.

Cialone, H. and Asaro, R. J. (1978) The role of hydrogen in the ductile fracture of plain carbon steels. *Metallic Transactions* **10A,** 367–375.

Davidson, D. L. (1991) Fracture characteristics of Al-4pct Mg Mechanically alloyed with SiC. *Metallic Transactions* **18A,** 2115–2128.

Dib, M. W. and Rodin, G. J. (1993) Three-dimensional analysis of creeping polycrystal using periodic arrays of truncated octahedrons. *Journal of the Mechanics and Physics of Solids* **41,** 725–748.

Ellyin, F. and Z. Xia (1993) A general theory of fatigue with the application to out-of-phase loading. *Journal of Engineering Materials Technology, Transactions ASME* **115,** 411–416.
Gurland, J. and Plateau, J. (1963) The mechanism of ductile rupture of metals containing inclusions. *Transactions ASM* **56,** 442–454.
Gurson, A. L. (1975) Plastic flow and fracture behaviour of ductile materials incorporating voids nucleation, growth and interaction. Ph.D. thesis, Brown University.
Hill, R. (1965) A self-consistent mechanics of composite materials. *Journal of the Mechanics and Physics of Solids* **13,** 213–222.
Kujawski, D., Xia, Z. and Ellyin, F. (1995) Morphology/loading direction coupling on the transverse behaviour of composites. In *Proceedings of the IUTAM Symposium on Microstructure-property Interactions in Composite Materials*, ed. R. Pyrz. Kluwer Academic Publishers, Netherlands, pp. 203–213.
Lamaitre, J. (1986) Local approach of fracture. *Engineering Fracture Mechanics* **25,** 523–537.
Li, C.-S. (1990) On the interaction among stage I short crack, slip band and grain boundary: a FEM analysis. *International Journal of Fracture* **43,** 227–239.
Li, C.-S. (1992) A three-dimensional finite element analysis for a crystallographic near the interface of an incompatible bicrystal. *Fatigue Fracture Engineering Material Structure* **16,** 21–35.
Li, C.-S. and Ellyin, F. (1994) Short crack trapping/untrapping in particle-reinforced metal matrix composites. *Composite Science and Technology* **52,** 117–124.
Li, C.-S. and Ellyin, F. (1996) On fatigue damage in particulate reinforced metal matrix composites. *Materials Science and Engineering* **A214,** 115–121.
Lin, C., Mayer, T. and Socie, D. (1992) Cyclic fatigue of alumina. ASTM STP1157, M. Mitchell and O. Buck, Eds., ASTM, Philadelphia, p. 527.
Lissenden, C. J. and Herakovich, C. T. (1996) Interfacial debonding in laminated titanium matrix composites. *Mechanics of Materials* **22,** 279–290.
Lloyd, D. (1991) Aspects of fracture in particulate reinforced metal matrix composites. *Acta Metallica Materials* **39,** 59–71.
Lloyd, D. (1995) Factors influencing the tensile ductility of melt processed particle reinforced aluminum alloys. In *Intrinsic and Extrinsic Fracture Mechanisms in Inorganic Composite Systems*, eds J. J. Lewandowski and W. H. Hunt, Jr., TMS Annual Meeting, Las Vegas, Nevada, pp. 39–47.
Marin, J. (1962) *Mechanical Behaviour of Engineering Materials*. Prentice-Hall Inc., Englewood Cliffs, New Jersey.
Mochida, T., Taya, M. and Lloyd, D. (1991) Fracture of particles in a particle/metal matrix composite under plastic straining and its effect on the Young's modulus of the composite, *Material Transactions* **JIM 12,** 931–942.
Nadai, A. (1950) *Theory of Flow and Fracture of Solid*, 2nd ed. McGraw-Hill, New York.
Nagpal, V., McClintock, F. A., Berg, C. A. and Subudhi, M. (1972) *Foundations of Plasticity*, ed. A. Sawczuk. Noordhoff, pp. 365–387.
Needleman, A. (1987) A continuum model for void nucleation by inclusion debonding. *ASME Journal of Applied Mechanics* **54,** 525–531.
Needleman, A. and Rice, J. R. (1978) Limits to ductility set by plastic flow localization. In *Mechanics of Sheet Metal Forming*, eds D. P. Koistinen and N.-M. Wang, Plenum Press, New York, pp. 237–265.
Ravichandran, G. and Liu, C. T. (1995) Modelling constitutive behaviour of particulate composite undergoing damage. *International Journal of Solids and Structures* **32,** 979–990.
Shi, N., Arsenault, R., Krawitz, A. and Smith, L. (1993) Deformation-induced residual stress changes in SiC whisker-reinforced 6061 Al composites. *Metallic Transactions* **24A,** 187–196.
Takehiro, I., Yoriko, O. and Kenji, W. (1995) Fracture strength evaluation of Zirconia particle-reinforced nickel matrix composites by disk-bending tests. *Journal of Japan Institute of Metals* **59,** 864–877.
Wienecke, H. A., Brockenbrough, J. R. and Romanko, A. D. (1995) A three-dimensional unit cell model with application towards particulate composites. *ASME Journal of Applied Mechanics* **62,** 136–140.
Xia, Z., Ellyin, F. and Meijer, G. (1997) Mechanical behaviour of Al_2O_3 particulate reinforced 6061 aluminum alloy under uniaxial and multiaxial cyclic loading. *Composite Materials Science and Technology* **37,** 237–248.